Analytica Chimica Acta 911 (2016) 59–68

Contents lists available at ScienceDirect

Analytica Chimica Acta

journal homepage: www.elsevier.com/locate/aca

An intimately bonded titanate nanotube–polyaniline–gold nanoparticle ternary composite as a scaffold for electrochemical enzyme biosensors

Xiaoqiang Liu [a, **], Jie Zhu [a], Xiaohe Huo [a], Rui Yan [a], Danny K.Y. Wong [b, *]

[a] Institute of Environmental and Analytical Sciences, College of Chemistry and Chemical Engineering, Henan University, Kaifeng, Henan Province, 475004, PR China

[b] Department of Chemistry and Biomolecular Sciences, Macquarie University, Sydney, NSW 2109, Australia

HIGHLIGHTS

- A ternary TiO_2 nanotube–polyaniline–gold nanoparticle composite was developed.
- New synthetic route for ternary composite with a polyaniline molecular wire between TiO_2 nanotubes and gold nanoparticles.
- An electrochemical biosensor with ternary composite as a scaffold.
- Ternary composite facilitated improved analytical performance of electrochemical biosensor.

GRAPHICAL ABSTRACT

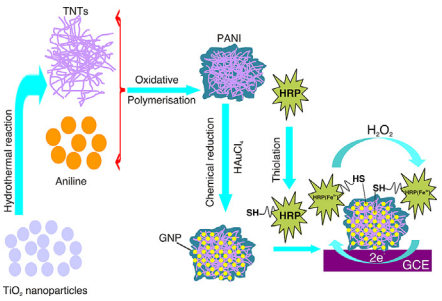

ARTICLE INFO

Article history:
Received 8 December 2015
Accepted 12 January 2016
Available online 27 January 2016

Keywords:
A TNT-PANI-GNP ternary composite
PANI molecular wire
Electrochemical enzyme biosensor
Horseradish peroxidase

ABSTRACT

In this work, titanate nanotubes (TNTs), polyaniline (PANI) and gold nanoparticles (GNPs) were assembled to form a ternary composite, which was then applied on an electrode as a scaffold of an electrochemical enzyme biosensor. The scaffold was constructed by oxidatively polymerising aniline to produce an emeraldine salt of PANI on TNTs, followed by gold nanoparticle deposition. A novel aspect of this scaffold lies in the use of the emeraldine salt of PANI as a molecular wire between TNTs and GNPs. Using horseradish peroxidase (HRP) as a model enzyme, voltammetric results demonstrated that direct electron transfer of HRP was achieved at both TNT-PANI and TNT-PANI-GNP-modified electrodes. More significantly, the catalytic reduction current of H_2O_2 by HRP was ~75% enhanced at the TNT-PANI-GNP-modified electrode, compared to that at the TNT-PANI-modified electrode. The heterogeneous electron transfer rate constant of HRP was found to be ~3 times larger at the TNT-PANI-GNP-modified electrode than that at the TNT-PANI-modified electrode. Based on chronoamperometric detection of H_2O_2, a linear range from 1 to 1200 μM, a sensitivity of 22.7 μA mM^{-1} and a detection limit of 0.13 μM were obtained at the TNT-PANI-GNP-modified electrode. The performance of the biosensor can be ascribed to the superior synergistic properties of the ternary composite.

1. Introduction

There have been many intensive studies on optoelectronic devices consisting of (photo)electrochemically active organic

* Corresponding author.
** Corresponding author.
E-mail addresses: liuxiaoqiang@henu.edu.cn (X. Liu), Danny.Wong@mq.edu.au (D.K.Y. Wong).

http://dx.doi.org/10.1016/j.aca.2016.01.024
0003-2670/

materials [1]. Among them, polyaniline (PANI) has been widely applied to the development of photovoltaic devices [2], electrochromic devices [3], lithium batteries [4], and gas sensors [5]. In these applications, the organic polymer PANI exhibits high electrical conductivity, strong photocatalytic capability and good environmental and thermal stability [6]. Notably, the oxidative polymerisation of aniline is known to form PANI with tuneable electrical conductivity, which is a desirable feature for practical (photo)electrochemical applications [7,8]. In general, chemically oxidised aniline in an acid solution will form a conductive emeraldine salt of PANI ($[C_6H_4NH]_2[C_6H_4N]_2)_n$; (ES)-PANI). ES-PANI can be further chemically or electrochemically converted to the highly oxidised pernigraniline $(C_6H_4N)_n$) or reduced to leucomeraldine $(C_6H_4NH)_n$) [7,8]. However, both pernigraniline and leucomeraldine are less conducting than ES-PANI and are therefore not ideal for use in the development of electrochemical sensing devices.

Recently, inorganic TiO_2 or $Na_2Ti_2O_4(OH)_2$ (titanate) nanomaterials have also been extensively applied to the construction of electrochemical and photoelectrochemical sensors to exploit their biocompatibility, chemical inertness, mechanical stability, photocatalytic ability, high porosity and large specific surface area [9,10]. For example, Xie et al. have synthesised nanosheet-based TiO_2 microspheres with a hollow core–shell structure and applied this nano-platform to the construction of a horseradish peroxidase (HRP) mediator-free biosensor [9]. While the excellent biocompatibility and porous geometry of this TiO_2 nano-material has facilitated direct electron transfer of HRP at the biosensor, the semiconducting TiO_2 exhibited low electrical conductivity (<0.1 S m^{-1}). Therefore, the synergistic application of TiO_2 and PANI, in which the respective attributes are integrated, will benefit the development of electrochemical biosensors [11].

In spite of the advantages of PANI and TiO_2 (or titanate), PANI-TiO_2 or PANI-titanate composite-based electrochemical biosensors have to-date not been reported. In fact, only one electrochemical glucose biosensor was developed by sequentially applying nanometer-sized TiO_2 and PANI on a glassy carbon electrode (GCE) [12]. In the detection of glucose, this biosensor showed a linear range between 0.02 mM and 6.0 mM, a sensitivity of 6.3 μA mM^{-1} cm^{-2} and a limit of detection of 18 μM. However, a deficiency in this work is the poor contact between PANI and TiO_2, which may have negatively affected the biosensor performance. In contrast, as reported by Kim et al. [13], chemical oxidation polymerisation of PANI on TiO_2, rather than a layer-by-layer assembly of TiO_2 and PANI, is an effective way to offer more intimate conduction through a larger contact area between PANI and TiO_2 nanomaterials for efficient interfacial charge transfer.

In comparison to TiO_2 nanoparticle-based biosensors, titanate nanotube (TNT)-based biosensors have dramatically improved performance arising from their large surface area, biocompatibility, conductivity and porous structure of tubular titanate [14]. The large surface area and porous structure of the TNT matrix aid in immobilising an appreciable load of biomolecules and providing a biocompatible microenvironment. In addition, the unique hollow structure of TNTs will potentially facilitate stable immobilisation of small biological molecules on the inner wall of the nanotubes. Therefore, a composite consisting of TNTs, instead of TiO_2 nanoparticles, and PANI is expected to further enhance the performance of the material.

Recently, gold nanoparticles (GNPs) immobilised on an electrochemical biosensor were demonstrated to not only increase the electrical conductivity, but also to improve the direct electron transfer between a biomolecule and the electrode [10]. For example, our group has previously employed a conventional chemical reduction method [10,14] and a photo-reduction method [14], respectively, to deposit GNPs on TNTs and applied them to the development of enzyme biosensors. However, we found such a simple reductive deposition of GNPs resulted in sparsely distributed GNP accumulations on the substrate material. Alternatively, the amino groups on PANI can be exploited as a chemical linker between GNPs and TNTs [15]. More specifically, by oxidatively polymerising aniline in a strong acid environment, the amino groups on PANI are easily protonated. Hence, the positively charged PANI will be electrostatically attracted to $AuCl_4^-$ to yield GNP conjugated PANIs. In this way, PANI can not only facilitate a well-dispersed, dense deposition of GNPs on TNTs and enhance the contact between GNPs and TNTs in a GNP-PANI-TNT composite, but also improve the conductivity of TNTs, which can benefit the performance, electrochemical and chemical stability of the ternary composite.

In the present work, a ternary composite consisting of TNTs, PANI and GNPs with improved conductivity was prepared and applied as a scaffold of an enzyme biosensor. In brief, TNTs were initially prepared by hydrothermally reacting TiO_2 nanoparticles with aqueous NaOH, followed by an *in situ* chemical oxidation polymerisation of aniline on TNTs to form a TNT-PANI composite. In this way, defects formed on TNTs will in turn offer a large surface support for amorphous PANI, while PANI will increase the conductivity and enhance the deposition of GNPs. Next, GNPs were deposited on the TNT-PANI surface using PANI as a linker. We expect these procedural steps will provide a more intimately bonded TNT-PANI-GNP structure, which will directly improve the analytical performance of a biosensor consisting of such a scaffold, compared to a previously reported layer-by-layer assembly of TNTs and GNPs [10,14]. The as-prepared composite of TNTs-PANI-GNPs, pure PANI and TNTs were all characterised by microscopic and spectroscopic techniques. To further enhance the stability and direct electron transfer of HRP at the biosensor interface, HRP molecules were thiolated using a dithio linker to enhance the contact between HRP and TNTs-PANI-GNPs through the strong interaction between the sulfhydryl groups and GNPs [16]. Finally, the TNT-PANI-GNP composite, the room temperature ionic liquid, 1-decyl-3-methylimidazolium bromide ([Demim]Br), and Nafion were assembled as a biosensor scaffold for immobilising the thiolated HRP on the electrode surface. In our work, [Demim]Br and Nafion acted as anchoring agents of the assembly on the electrode surface. The electrochemical behaviour, analytical performance, precision and stability of the TNT-PANI-GNP, TNT-PANI and TNT modified HRP biosensors were then systematically investigated.

2. Experimental

2.1. Materials and reagents

Aniline monomer (99.5% purity) and ammonium persulfate (98% purity) were purchased from J&K Scientific Ltd., Beijing, China. TiO_2 nanoparticles (type P25) were obtained from Tianjin Chemical Reagent Co. Ltd., China. HRP, *n*-succinimidyl 3-(2-pyridyldithio) propionate (SPDP), dithiothreitol (DTT), ethylene diamine tetraacetic acid (EDTA), bicinchoninic acid (BCA) QuantiPro Protein Assay Kit, [Demim]Br, $HAuCl_4 \cdot 3H_2O$ and dimethylsulfoxide (DMSO) were purchased from Sigma–Aldrich, USA. Zeba spin desalting columns were purchased from Thermo Fisher Scientific Inc. All solutions were prepared in Milli-Q ultrapure water.

2.2. Apparatus

Electrochemical measurements were performed using a CHI630C electrochemical workstation (CH Instruments, Shanghai, China) with a conventional three-electrode system consisting of a modified 3-mm diameter GCE, a platinum wire counter electrode

and a Ag|AgCl (3.0 M KCl) reference electrode. All electrodes were purchased from Gaozhiruilian Co. Ltd., Wuhan, China. The chemical composition of the composites was investigated by X-ray diffraction (XRD, X-PertPro, Netherland) with a Cu Kα radiation (λ = 1.5406 nm) and Fourier transform infrared spectroscopy (FT-IR, Nicolet 170, USA). Electrochemical impedance spectroscopy (EIS) was conducted using an IM6ex electrochemical workstation (Zahner, Germany). The morphology and chemical composition of the prepared nano-materials were characterised by transmission electron microscopy (TEM) (Tecnai G2 20, USA), selected area electron diffraction (SAED) (Tecnai G2 20, USA), scanning electron microscopy (SEM) (JSM-7500F, JEOL, Japan) and energy dispersive X-ray (EDX) (JSM-7500F, JEOL, Japan).

2.3. Preparation of TNT-PANI-GNP composites

TNTs were prepared by initially delivering a mixture of 0.6 g TiO_2 nanoparticles and 120 mL (10 M) aqueous NaOH to a Teflon-lined autoclave for a hydrothermal reaction at 120 °C for 48 h. A white coloured crude product obtained was washed with 0.1 M HCl three times, and then adjusted with distilled water to achieve pH 7. The product was again washed with Milli-Q water three times, followed by centrifugation and drying in a 60 °C oven for 2 h. The product of TNTs was then ground to a powder.

Initially, a TNT-PANI composite was synthesised by stirring, using a magnetic stirrer, a mixture of 0.3 g TNTs, 4.83 mL aniline hydrochloride solution (0.1 M) and 10 mL HCl solution (0.1 M) in a reaction vessel placed in an ice water bath for 1 h to obtain a uniform suspension. Next, a second 4.83-mL ammonium persulfate aliquot (0.1 M) was added dropwise to the well-dispersed suspension over a 2-h duration with continuous stirring at 0–5 °C. The mixture was allowed to react in an ice bath for another 3 h before a dark green precipitate was obtained. The solution was left undisturbed at 4 °C overnight to facilitate complete chemical reaction. The dark green precipitate was then repeatedly washed with Milli-Q water until pH 7 was achieved. Finally, the product was dried at 60 °C for 2 h before it was ground to a powder.

In preparing the TNT-PANI-GNP composite, a suspension of 18 mg TNTs-PANI in 18 mL Milli-Q water was sonicated to obtain a homogeneous dark green solution. Then, 1 mL $HAuCl_4$ (0.01 M) and 1 mL sodium citrate (0.01 M) were added and stirred. Next, 1 mL icy cold and freshly prepared $NaBH_4$ solution (0.1 M) was added to the solution with stirring. Herein, citrate serves as a capping agent because it cannot reduce the gold salt at room temperature (25 °C). The solution was stirred for 0.5 h at room temperature before it was left undisturbed for a night. The final product was centrifuged and sequentially washed with Milli-Q water and ethanol, before it was dried in a 60 °C vacuum overnight.

2.4. Thiolation of HRP

In the thiolation procedure, 1 mg SPDP was initially dissolved in 160 μL DMSO. Then, 12.5 μL of this SPDP solution (20 mM) and 1 mg HRP were added to 500 μL phosphate buffered saline (PBS) containing 1 mM EDTA. This mixture was allowed to react for 30–60 min at room temperature to obtain SPDP-modified HRP. Desalt spin columns (that can directly purify, desalt and buffer-exchange protein samples, and thus circumventing any chromatographic system, cumbersome preparation and equilibration procedures) were centrifuged at 2500 rpm for 5 min to remove storage solution and then exchanged using acetate buffer 2–3 times to equilibrate them. The SPDP-modified HRP was then introduced in a desalt spin column, which was centrifuged to remove reaction by-products and unreacted SPDP. Next, 200 μL DTT solution was added to 500 μL of SPDP-modified HRP solution, followed by a 30-min incubation to produce thiolated HRP. Finally, PBS-EDTA was employed to equilibrate the desalting columns, and thiolated HRP was desalted using the equilibrated columns to remove the excess DTT. The concentration of thiolated HRP was determined by estimating the quantity of residual protein content in the final solution using a BCA-based QuantiPro Protein Assay Kit, as previously reported by Fowler et al. [16]. By assessing the UV absorbance difference of pyridine-2-thione before and after DTT cleavage, the molar ratio of SPDP to HRP was estimated to be ~3.9.

2.5. Preparation of thiolated HRP modified electrodes

A 3-mm diameter GCE was polished using 0.3 μm alumina powder, and then sequentially washed with deionised water and ethanol before being dried at room temperature. A mixture consisting of 300 μL of HRP solution (2 mg mL^{-1}), 20 mg of TNTs-PANI-GNPs, 4 mg of [Demim]Br and 50 μL Nafion (5%) was agitated at 4 °C in a full temperature oscillation incubator for 4 h. Then, a TNT-PANI-GNP|[Demim]Br|Nafion|HRP|GCE was prepared by applying 4 μL of the suspension on the GCE. A similar procedure involving mixing of 20 mg of TNTs-PANI with 300 μL of HRP solution, 4 mg of [Demim]Br and 50 μL Nafion was adopted to prepare a TNT-PANI|[Demim]Br |Nafion|HRP|GCE.

2.6. Electrochemical measurements

During electrochemical measurements, all working solutions were deoxygenated by nitrogen gas for 15 min and a nitrogen atmosphere was maintained over the solutions. In amperometry, a constant potential of −0.4 V was applied to the working electrode. A current response was recorded after acquiring a stable baseline signal following an injection of H_2O_2 into the electrochemical cell. EIS was performed in the presence of 5.0 mM $K_3[Fe(CN)_6]$ and 5.0 mM $K_4[Fe(CN)_6]$ in 0.1 M KCl with an AC peak-to-peak voltage amplitude of 4 mV superimposed on the half-wave DC potential of 0.28 V over a frequency range from 100 kHz to 1 mHz. All results obtained were presented as Nyquist plots and fitted with a SIM software associated with the IM6ex impedance analyser (Zahner, Germany).

3. Results and discussion

3.1. Characterisation of the TNTs, PANI, TNT-PANI and TNT-PANI-GNP composites

In this work, a ternary TNT-PANI-GNP nanocomposite was developed. Before applying the nanocomposite as a scaffold on a biosensor, we have characterised the surface chemistry of the nanocomposite using a range of spectroscopic techniques. The morphology of TNTs, TNTs-PANI and TNTs-PANI-GNPs was initially examined by FETEM and the micrographs obtained are shown in Fig. 1(A)a, b and c, respectively. In Fig. 1(A)a, the well-separated TNTs show a relatively uniform geometrical dimension with a mean diameter of approximately 8–10 nm and length of a few hundred nm, indicating the nanoscale of TNTs. The inset in Fig. 1(A)a is a magnified portion of a, from which the wall thickness of the TNTs was estimated to be 1.5 nm. In Fig. 1(A)b, the TNTs appear to be enclosed by semitransparent amorphous PANI and they tend to stack together, demonstrating that PANI was polymerised on top of TNTs [17]. In Fig. 1(A)c, the GNPs that appear as dark spheres are observed to be quite evenly dispersed in the TNT-PANI matrix and are well separated from each other, indicating the successful reduction deposition of nano-gold on TNTs-PANI. A magnified portion of Fig. 1(A)c, shown in Fig. 1(A)d, presents a clearer image of the TNT-PANI-GNP composite. This was used to estimate the

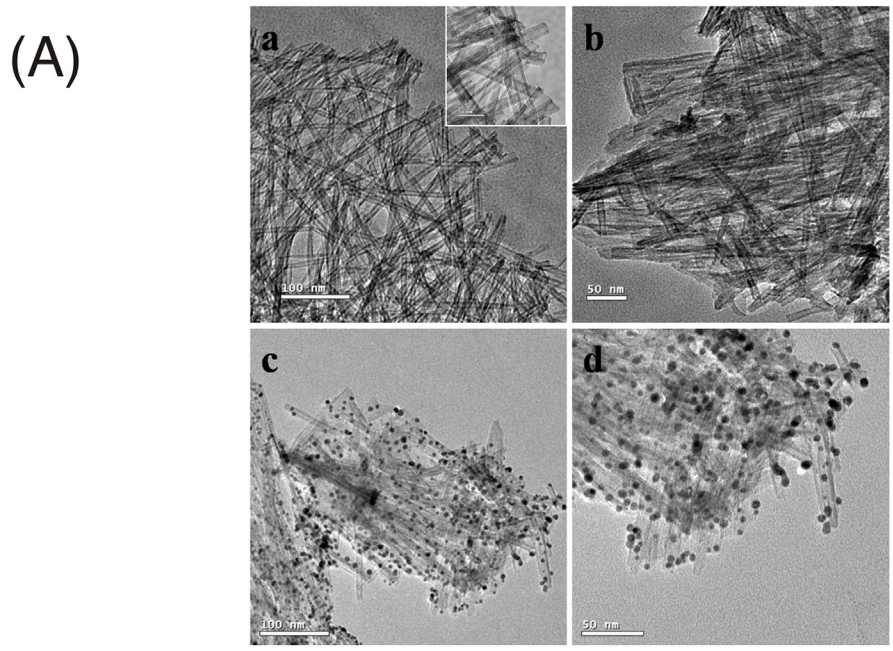

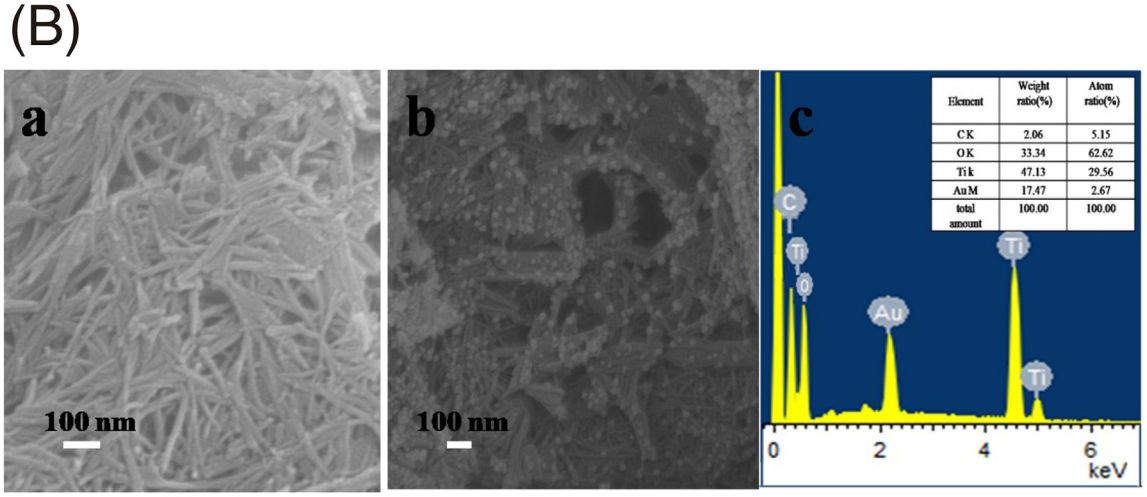

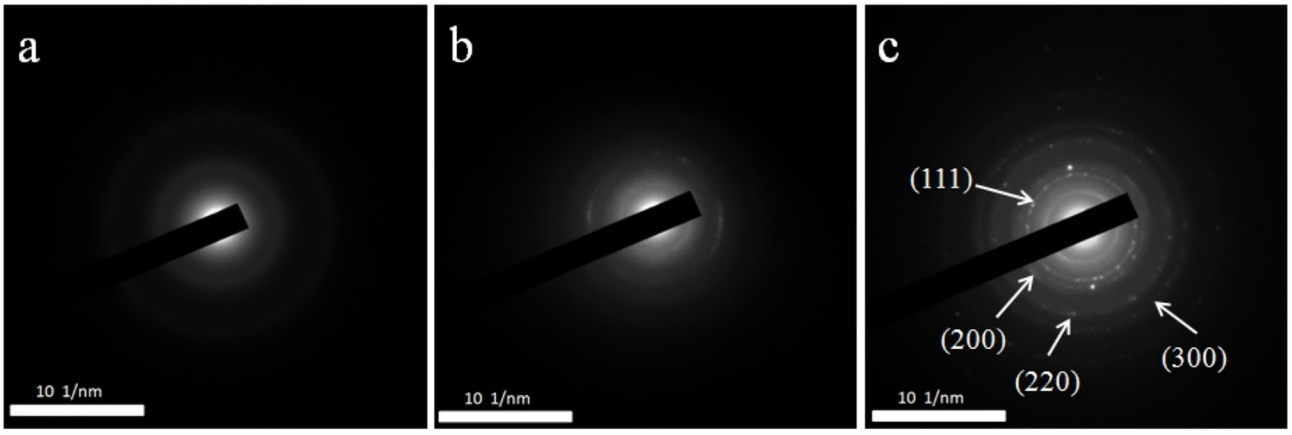

Fig. 1. (A) Transmission electron micrographs of (a) TNTs, (b) TNT-PANI (c) and (d) TNT-PANI-GNP composite at different scales; (B) (a)scanning electron micrograph of a TNT-PANI composite, (b) scanning electron micrograph of a TNT-PANI-GNP composite and (c) EDX spectrum of a TNT-PANI-GNP composite; (C) SAED patterns of (a) PANI, (b) TNT-PANI and (c) TNT-PANI-GNP composite.

average particle size of GNPs as 5–8 nm.

The scanning electron micrographs of TNTs-PANI and TNTs-PANI-GNPs are used to further confirm the formation of the binary and ternary nanocomposites. The micrograph of TNTs-PANI (Fig. 1(B)a) displays long tubular structures with<12 nm diameters and several hundred nm axial lengths, which are consistent with the dimensions estimated based on TEM results shown in Fig. 1(A)a. However, PANI is not clearly observable in this figure, most likely because of the semitransparent amorphousness of PANI. In Fig. 1(B)b, spherical particles, assumed to be GNPs, of ~8–10 nm average particle size were deposited on TNTs-PANI without noticeable agglomeration. EDX spectrum shown in Fig. 1(B)c was also used to investigate the elemental composition of TNTs-PANI-GNPs. In this spectrum, the Ti and O peaks originated from TNTs and the peak of C are attributed to PANI [18]. Most importantly, an Au peak appearing at ~2.10 keV, contributed ~17.5% weight to the ternary composite. The EDX results are therefore in agreement with those obtained using TEM and SEM, supporting the successful preparation of the ternary composite.

SAED was used to characterise the crystalline nature of PANI, the TNT-PANI and TNT-PANI-GNP composite. In Fig. 1(C)a, the SEAD pattern of PANI displays some diffuse and blurry rings, indicative of the amorphous phase of the external structure of HCl doped-PANI [19,20]. On the contrary, as shown in Fig. 1(C)b, clearer and more distinct rings appeared in the SEAD pattern of the PANI-TNT composite, which is attributed to the reflection of polycrystalline TNT structure [21]. After the reduction of $AuCl_4^-$ on PANI-TNT, four visibly bright circular rings are observed in the corresponding SAED pattern of the ternary composite, as displayed in Fig. 1(C)c. This is in agreement with results obtained in characterising gold nanoparticle-doped lead lanthanum [22,23], where several clear and bright rings in the SAED patterns of GNPs were labelled as (111), (200), (220) and (311) reflections. Accordingly, the four rings displayed in Fig. 1(C)c are indicative of the presence of pure crystalline gold nanoparticles in the ternary composite.

The corresponding characteristic X-ray diffraction patterns of PANI (trace a), TNTs (trace b), TNTs-PANI (trace c) and TNTs-PANI-GNPs (trace d) are displayed in Fig. 2(A). In trace a, PANI exhibited a typical 2θ crystalline peak at 25.2° and two characteristic amorphous peaks at approximately 15.1° and 20.5°, which are in agreement with the XRD pattern of ES-PANI reported by Srivastava et al. in characterising a TiO_2-doped polyaniline composite for hydrogen gas sensing [24]. We use this as a support for the formation of ES-PANI in our work. According to Srivastava et al., the intensity of the crystalline peak at 25.2° is noticeably larger than the amorphous peaks, indicating that ES-PANI is not fully amorphous. The partial crystallinity of ES-PANI, originated from π-π interchain stacking, has resulted in an improved charge transfer capability and therefore electrical conductivity, which will benefit the development of electrochemical and photoelectrochemical biosensors [25,26]. In trace b, the 2θ diffraction peaks at 9.6°, 24.7°, 28.3°, 48.9° and 61.8° are assigned to (200), (110), (600), (020) and (002) crystal planes of orthorhombic TNTs, by comparing to the XRD spectra of the same type of TNTs synthesised previously [27,28]. These peaks ascribed to TNTs are also clearly observable in the XRD pattern in trace c, in addition to the two minor peaks at ~15.6° and 20.5° that originated from ES-PANI, indicating the formation of the TNT-PANI composite. Notably, the 2θ peaks arising from the TNT crystal planes have slightly shifted to 9.5°, 24.9°, 27.9°, 48.8°, and 63.1°, respectively, owing to the crystal change caused by the strong interaction between PANI and TNT. In trace d, the peaks at ~38.6°, 44.8°, 64.9°, and 77.8° are assigned to (110), (200), (220), and (311) reflection of gold nanoparticles, which are consistent with the 2θ peak position of gold nanoparticles synthesised by Paramasivam et al. [29]. In addition to the 2θ peaks assigned to

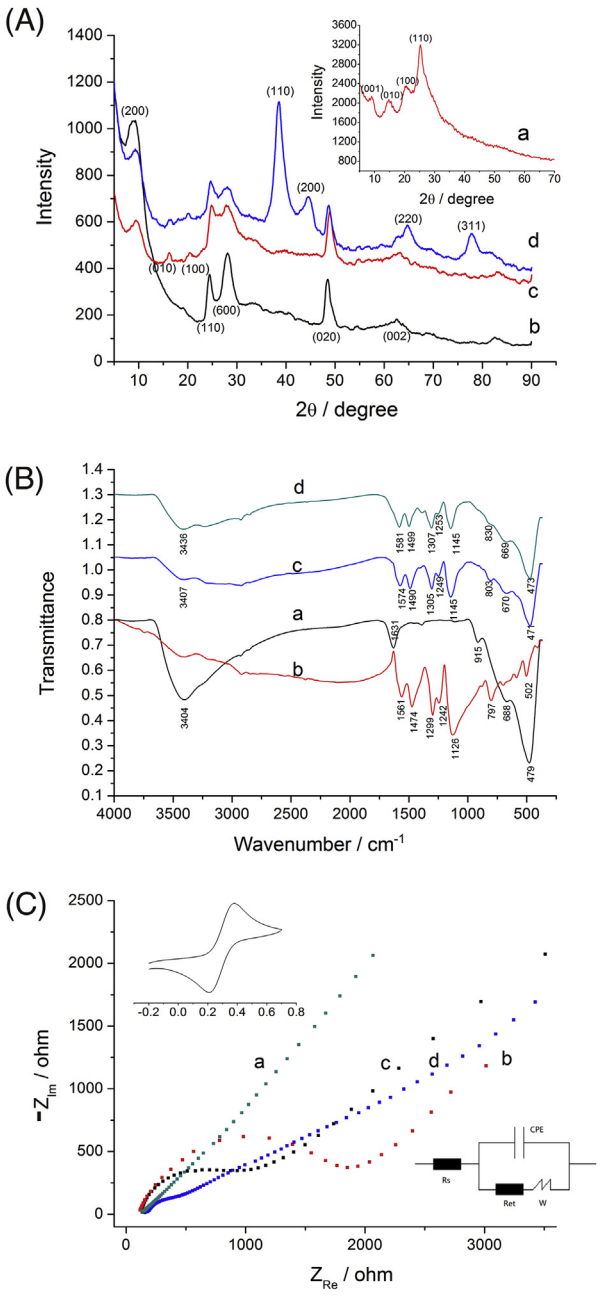

Fig. 2. (A) XRD pattern of (a) PANI, (b) TNTs, (c) TNTs-PANI and (d) TNTs-PANI-GNPs; (B) FT-IR spectra of (a) TNTs, (b) PANI, (c) TNTs-PANI, and (d) TNTs-PANI-GNPs; (C) Nyquist plots of 5.0 mM $[Fe(CN)_6]^{3-}$ and 5.0 mM $[Fe(CN)_6]^{4-}$ at (a) a bare GCE, (b) a TNT|[Demim]Br|Nafion|GCE, (c) a TNT-PANI| [Demim]Br|Nafion|GCE and (d) a TNT-PANI-GNP |[Demim]Br|Nafion|GCE in 0.1 M KCl. The two insets respectively show the cyclic voltammogram of 5.0 mM $[Fe(CN)_6]^{3-}$ and 5.0 mM $[Fe(CN)_6]^{4-}$ at a TNT-PANI-GNP |[Demim]Br|Nafion|GCE in 0.1 M KCl and the equivalent circuit used in the computer simulations of the experimental impedance plots.

GNPs, all the peaks in trace c are also identifiable in trace d, demonstrating that GNPs were successfully deposited on the TNT-PANI surface.

Next, FT-IR was conducted to gain structural information of TNTs, PANI, TNTs-PANI and TNTs-PANI-GNPs and the corresponding spectra obtained are displayed as trace a, b, c and d in Fig. 2(B). In these traces, the O–H stretching vibration from surface hydroxyl on all the materials has produced the broad absorption from 3000 to 3700 cm^{-1} [30]. In trace a, the Ti–O stretching and Ti–O–Ti

bridging vibration can be represented by the low frequency absorption at 400-700 cm^{-1}, which is a characteristic absorption of TiO_2 or titanate nanomaterials [31]. In trace b, the peak at 1242 cm^{-1} is attributed to C–N^{+}• stretching vibration in ES-PANI [32]. The peaks at 1299, 1126 and 797 cm^{-1} correspond to the C–N stretching of the secondary aromatic amine, the N = Q = N (Q represents the quinoid ring) stretching and the aromatic C–H out-of-plane bending vibration [33]. The peaks at 1561 cm^{-1} and 1474 cm^{-1} are ascribed to the C=C stretching vibration of quinoid and benzenoid rings, respectively [34]. All these characteristic absorption peaks arise from the highly electrical conductive ES-PANI [33,35]. As shown in trace c, both the characteristic bands of PANI (700-1600 cm^{-1}) and the absorption band attributable to Ti–O–Ti and Ti–O vibration (400-700 cm^{-1}) are clearly observable, indicating successful formation of the PANI-TNT composite. In the FT-IR spectrum of PANI-TNTs, characteristic PANI absorption peaks at 1561, 1474, 1299 and 1126 cm^{-1} (shown in trace b), corresponding to the stretching mode of C=C, C–N and N = Q = N bands, have respectively shifted to 1574, 1490, 1305 and 1145 cm^{-1} (in trace c). We interpreted this as the result of strong bonding formed between nitrogen atoms in PANI and titanate during the polymerisation step [36]. This strong bonding would restrict the PANI chain vibration and the electron attracting capability of titanate may then delocalise some of the electrons around the nitrogen in PANI, which will likely lead to the shifts of the FT-IR peaks of PANI to higher wavenumbers [7]. The deposition of GNPs on the TNT-PANI has resulted in further positive shift of the stretching mode of C=C, C–N and N = Q = N bands, as shown in trace d, which is most likely caused by the strong interaction between GNPs and ES-PANI [37]. The OH stretching band of TNTs-PANI-GNPs has increased by 32 cm^{-1} compared to that of TNTs-PANI. This shift is probably induced by the cleavage of OH groups from TNTs following the deposition of GNPs [38].

EIS of $[Fe(CN)_6]^{3-/4-}$ was also used to study the surface features of the four electrodes, (a) a bare GCE, (b) a TNT modified GCE, (c) a TNT-PANI modified GCE and (d) a TNT-PANI-GNP modified GCE. In this experiment, an AC potential of 4 mV was superimposed on the half-wave potential of 0.28 V (see cyclic voltammogram of 5.0 mM $[Fe(CN)_6]^{3-}$ and 5.0 mM $[Fe(CN)_6]^{4-}$ in 0.1 M KCl in the inset of Fig. 2(C)). The AC current was then measured to calculate the impedance over the 100 kHz–1 mHz frequency range. The corresponding imaginary impedance (Z_{IM}) versus real impedance (Z_{Re}) Nyquist plots obtained are shown in Fig. 2(C). A semicircle in the high frequency region and a straight line in the low frequency region are generally displayed in these Nyquist plots, indicating a mixed electron transfer and diffusion control mechanism for the $[Fe(CN)_6]^{3-/4-}$ reaction at an electrode surface. The diameter of a semicircle represents the interfacial electron transfer resistance (R_{et}) of the redox probe at the modified electrode surface. Notably, the Nyquist plot obtained at the bare electrode (trace a) exhibited a nearly straight line with an indistinguishable semicircle, showing an almost complete diffusion-control process and thus the best conductivity of the bare electrode among these electrodes. Based on an equivalent circuit (shown in the inset of Fig. 2(C)) consisting of a constant phase element (CPE; which has incorporated the Helmholtz double layer and surface roughness or heterogeneity of the electrode) in parallel arrangement with both a R_{et} and a Warburg diffusion impedance (Z_W), which is then in series with a solution resistance (R_S), theoretical Nyquist plots were generated by optimising the parameters of these circuit elements to fit the experimental Nyquist plots. In this way, R_{et} was estimated to be 255 Ω at the TNT-PANI-GNP|GCE, 755 Ω at the TNT-PANI|GCE and 1735 Ω at the TNT|GCE. As expected, the incorporation of both PANI and GNPs enhances electrical conductivity of the composite, resulting in the lowest R_{et} at the TNT-PANI-GNP modified electrode.

In summary, the characterisation results have supported strong interaction or chemical bonding formation between TNTs, PANI and GNPs, which is expected to enhance the electrochemical characteristics and chemical stability of the ternary composite. According to previous reports [39], during the hydrothermal process, the TiO_2 nanoparticles were firstly converted into planar fragments after reacting with concentrated NaOH solution. A monolayer nanotube was obtained through the covalent bonding and intermolecular force between the end groups of TiO_2 planar fragments. Using the monolayer as a template, multilayer TiO_2 nanotubes were grown and and this eventually constituted to the formation of $Na_2Ti_2O_4(OH)_2$. We will next immobilise the ternary composite as a scaffold for immobilising HRP on a GCE for the catalytic reaction of H_2O_2. The analytical application of the modified GCE to the detection of H_2O_2 will then be conducted.

3.2. Electrochemical characterisation and analytical applications of modified electrodes

Fig. 3(A) shows the cyclic voltammograms of 50 mM N_2-saturated PBS obtained at a TNT-PANI-GNP|[Demim]Br|Nafion|GCE (trace a), a TNT-PANI|[Demim]Br|Nafion|HRP|GCE (trace b) and a TNT-PANI-GNP|[Demim]Br |Nafion|HRP|GCE (trace c). A featureless background voltammogram was observed at the TNT-PANI-GNP|[Demim]Br|Nafion|GCE, indicating that the TNT-PANI-GNP composite will not introduce any electrochemical interference to the measurement when it is used as a biosensor scaffold. In PBS alone, an irreversible reduction peak current appeared at ~−0.15 V was obtained in both trace b and c, which has mostly likely arisen from the direct electron transfer of HRP at both the TNT-PANI|[Demim]Br|Nafion|HRP|GCE and TNT-PANI-GNP|[Demim]Br|Nafion|HRP|GCE. Noticeably, the corresponding reduction current at the TNT-PANI-GNP |[Demim]Br|Nafion|HRP|GCE has increased by ~61.7% compared to that at the TNT-PANI|[Demim]Br|Nafion|HRP|GCE, which indicated that the TNT-PANI-GNP matrix has facilitated the direct electron transfer of HRP.

Fig. 3(B) shows the voltammograms of 1.0 mM H_2O_2 in 50 mM N_2-saturated PBS at (a) a TNT-PANI|[Demim]Br|Nafion|HRP|GCE and (b) a TNT-PANI-GNP|[Demim]Br|Nafion|HRP|GCE. The catalytic mechanism of HRP to H_2O_2 has previously been described by a series of reactions shown below [40].

$$\mathrm{HRP}\left(\mathrm{Fe}^{3+}\right) + \mathrm{H_2O_2} \rightarrow \mathrm{Compound\ I}\left(\mathrm{Fe}^{4+}=\mathrm{O}\right) + \mathrm{H_2O} \quad (1)$$

$$\mathrm{Compound\ I}\left(\mathrm{Fe}^{4+}=\mathrm{O}\right) + \mathrm{e}^{-} + \mathrm{H}^{+} \rightarrow \mathrm{Compound\ II} \quad (2)$$

$$\mathrm{Compound\ II} + \mathrm{e}^{-} + \mathrm{H}^{+} \rightarrow \mathrm{HRP}\left(\mathrm{Fe}^{3+}\right) + \mathrm{H_2O} \quad (3)$$

In this mechanism, HRP(Fe^{3+}) is firstly converted to Compound I ("Fe^{4+}=O" denotes oxyferrite) by the oxidation of H_2O_2 (Equation (1)). Compound I is then reduced back to HRP(Fe^{3+}) after successively gaining two electrons from the electrode, as shown in Equations (2) and (3).

Accordingly, in both voltammograms displayed in Fig. 3(B), a catalytic reduction peak observed at −0.1 V is attributed to the electrocatalytic of H_2O_2 by HRP. However, the catalytic reduction current towards H_2O_2 was ~75% higher at the TNT-PANI-GNP|[Demim]Br|Nafion|HRP|GCE (trace b) compared to that at the TNT-PANI| [Demim]Br|Nafion|HRP|GCE (trace a), demonstrating the superior conductivity and biocompatibility associated with the TNT-PANI-GNP composite as a biosensor scaffold over the TNT-PANI composite. Clearly, this enhancement is partly facilitated by the

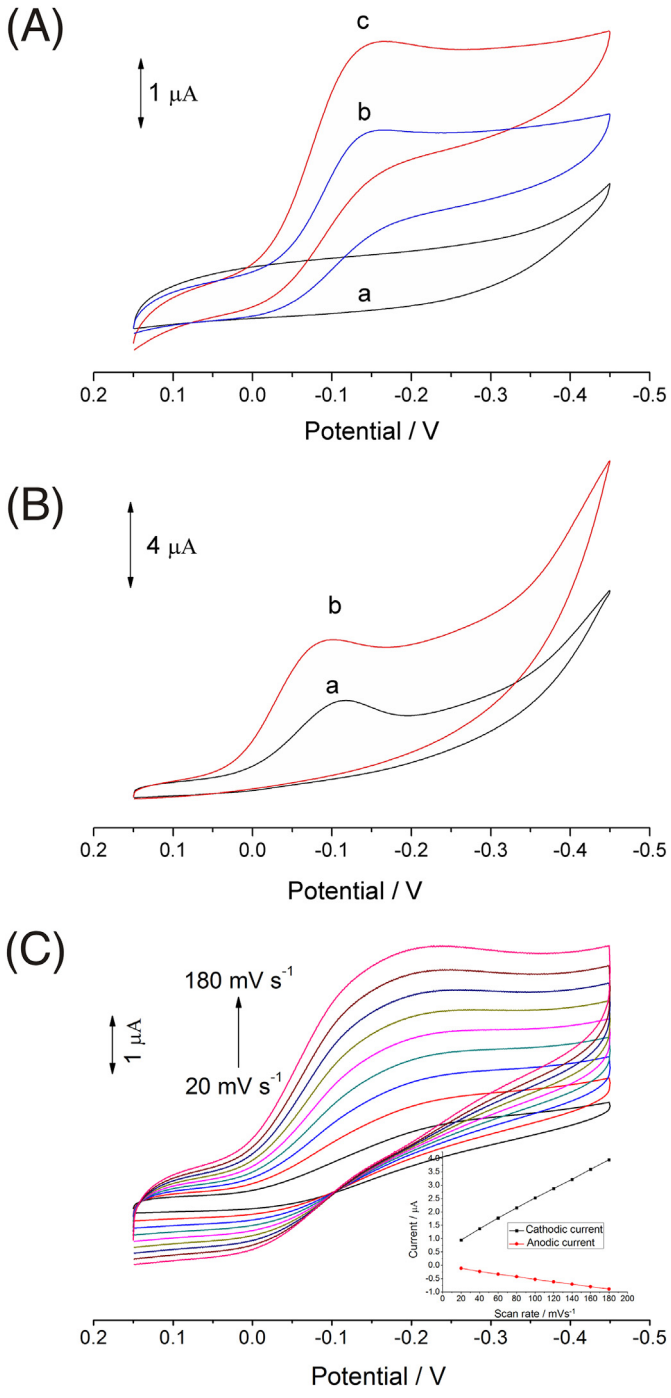

Fig. 3. (A) Cyclic voltammograms at (a) a TNT-PANI-GNP|[Demim]Br|Nafion|GCE, (b) a TNT-PANI|[Demim]Br|Nafion|HRP|GCE and (c) a TNT-PANI-GNP |[Demim]Br|Nafion|HRP|GCE in 50 mM N_2-saturated PBS (pH 7.0); scan rate: 100 mV s^{-1}; (B) cyclic voltammograms of 1.0 mM H_2O_2 at (a) a TNT-PANI |[Demim]Br|Nafion|HRP|GCE and (b) a TNT-PANI-GNP|[Demim]Br|Nafion |HRP|GCE in 50 mM N_2-saturated PBS (pH 7.0); scan rate: 100 mV s^{-1}; (C) Cyclic voltammograms of 0.1 M N_2-saturated PBS (pH7) at a TNT-PANI-GNP|[Demim]Br|Nafion|HRP|GCE at scan rates ranging from 20 to 180 mV s^{-1}; left inset shows a cathodic peak current versus scan rate plot and right inset shows an anodic peak current versus scan rate plot.

direct electron transfer of HRP, which has in turn aided the redox reaction between HRP(Fe^{3+}) and H_2O_2 in Equation (1) above.

Cyclic voltammetry of HRP at a TNT-PANI-GNP|[Demim]Br|Nafion|HRP|GCE was conducted with increasing scan rates (20–180 mV s^{-1}) to study the electron transfer of HRP at the ternary composite modified GCE. The voltammograms obtained are displayed in Fig. 3(C). The inset of Fig. 3(C) shows that both the cathodic (I_{pc}) and anodic peak currents (I_{pa}) increased linearly with the scan rates, implying a surface-controlled quasi-reversible process at the electrode surface. Using the Laviron equation,

$$logk_s = \alpha log(1-\alpha) + (1-\alpha)log\alpha - log\frac{RT}{nF\nu} - \frac{\alpha(1-\alpha)nF\Delta E_p}{2.3RT}$$

where α is charge transfer coefficient, v is the scan rate, *n*, *R*, *T* and *F* have their usual electrochemical meaning, α (0.52) was initially estimated from the slope of an anodic peak potential (E_p) versus log ν plot and a cathodic peak potential versus log ν plot. By substituting α into the Laviron equation, the heterogeneous electron transfer rate constant, k_s, of HRP at the TNT-PANI-GNP modified GCE was estimated to be 4.1 s^{-1} at 100 mV s^{-1}, which is ~3 times faster than 1.3 s^{-1} at a TNT-PANI modified biosensor. The above results indicated that the direct electron transfer of HRP was significantly improved at ternary composite modified electrodes compared to that at the TNT-PANI modified electrodes.

The analytical performance of the TNT-PANI-GNP|[Demim]Br|Nafion|HRP|GCE (trace a), TNT-PANI|[Demim]Br|Nafion|HRP|GCE (trace b) and TNT|[Demim]Br|Nafion|HRP|GCE (trace c) was evaluated using chronoamperometry. Based on the cyclic voltammograms in Fig. 3(B), a constant potential of −0.4 V was selected for use in the chronoamperometric experiment. Here, a 50-μL aliquot of 35 mM H_2O_2 was added to 50 mM PBS (pH7.0) with moderate stirring. As shown in Fig. 4(A), the amperometric responses at the TNT-PANI-GNP|[Demim]Br|Nafion|HRP|GCE (trace a) and the TNT-PANI|[Demim]Br|Nafion|HRP|GCE (trace b) increased stepwise with successive additions of H_2O_2, while that at the TNT|[Demim]Br|Nafion|HRP|GCE (trace c) displays indistinguishable enhancement after each addition. Furthermore, the current at the TNT-PANI-GNP|[Demim]Br|Nafion|HRP|GCE (trace a) is ~57% larger than that at the TNT-PANI biosensor (trace b) at the same H_2O_2 concentration, demonstrating a degree of higher detection capability at the former biosensor over that of the latter. The inset in Fig. 4(A) shows the enlarged chronoamperometric responses at the TNT-PANI-GNP |[Demim]Br|Nafion|HRP|GCE recorded for the first four additions of H_2O_2. Fig. 4(B) shows the corresponding calibration plots obtained based on the currents at (a) the TNT-PANI-GNP|[Demim]Br|Nafion|HRP|GCE and (b) the TNT-PANI |[Demim]Br|Nafion|HRP|GCE versus H_2O_2 concentration in the solution. At the TNT-PANI-GNP|[Demim]Br|Nafion|HRP|GCE (trace a), the calibration plot between 1 and 1200 μM can be represented by the following linear relationship (with a correlation coefficient of 0.993 (N = 25) that was found to be statistically significant at the 95% confidence level):

$$\text{Peak current}/\mu A = 22.7 \pm 0.157/\mu A\ mM^{-1}\ [H_2O_2] + (1.87 \pm 0.105)$$

where the uncertainties represent the 95% confidence intervals. Based on a signal-to-noise ratio of 3, the detection limit was estimated to be 0.13 μM.

The calibration plot (with a correlation coefficient of 0.994 (N = 18) that is also statistically significant at the 95% confidence level) for the TNT-PANI|[Demim]Br|Nafion|HRP|GCE (trace b) can be expressed as:

$$\text{Peak current}/\mu A = 12.6 \pm 0.146/\mu A\ mM^{-1}\ [H_2O_2] + (1.41 \pm 0.0925)$$

Accordingly, a linear range from 58 μM to 1050 μM and a detection limit of 2.6 μM were achieved at this biosensor.

In summary, the analytical performance of the TNT-PANI-GNP|[Demim]Br|Nafion|HRP|GCE has shown advantages over that of the

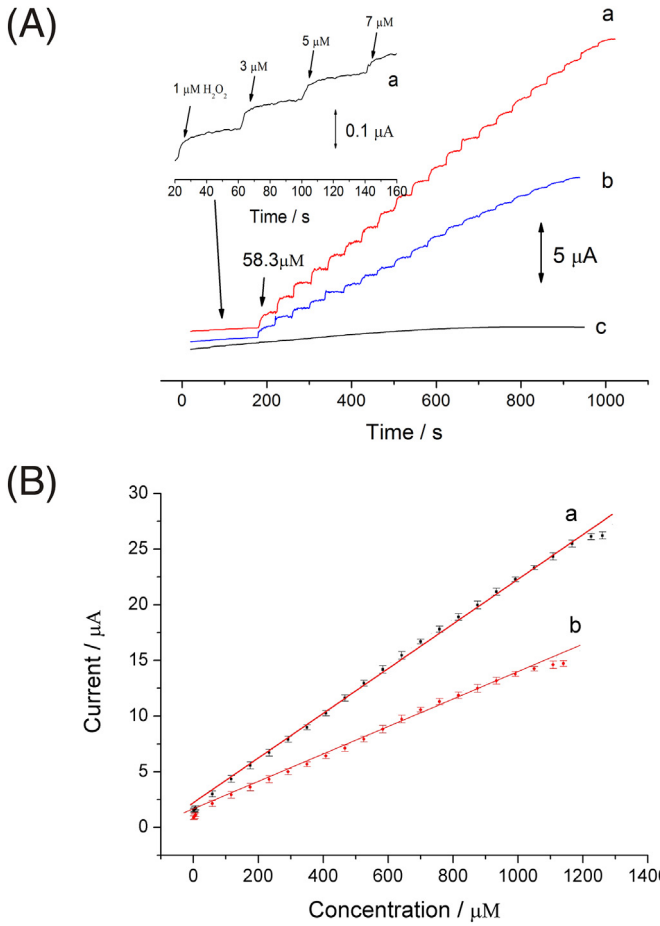

Fig. 4. (A) Chronoamperometric responses of successively added H_2O_2 at (a) a TNT-PANI-GNP|[Demim]Br|Nafion|HRP|GCE, (b) a TNT-PANI|[Demim]Br|Nafion|HRP|GCE and (c) a TNT|[Demim]Br|Nafion|HRP|GCE in 50 mM PBS (pH 7.0) at the operating potential of −0.4 V. Inset: magnified chronoamperometric responses of the first four successive H_2O_2 additions at a TNT-PANI-GNP |[Demim]Br|Nafion|HRP|GCE. (B) The H_2O_2 reduction current versus H_2O_2 concentration calibration plot at (a) a TNT-PANI-GNP|[Demim]Br |Nafion|HRP|GCE and (b) a TNT-PANI|[Demim]Br|Nafion|HRP|GCE.

TNT modified biosensor. A comparison of the analytical performance to other HRP biosensor is presented in Table 1, highlighting the excellent properties of PANI and GNPs. In particular, the

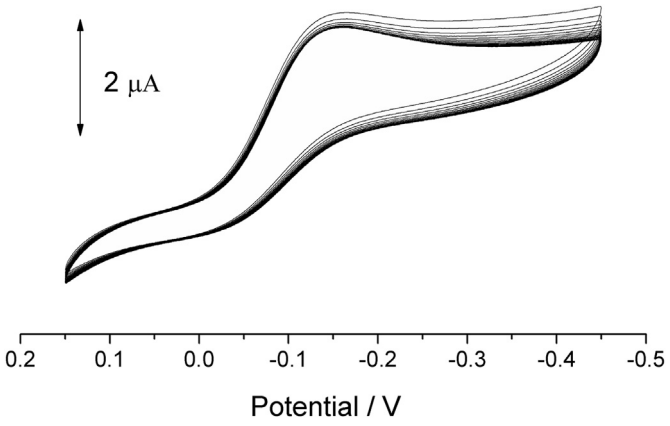

Fig. 5. Twenty continuous cyclic voltammograms at a TNT-PANI-GNP|[Demim]Br |Nafion|HRP|GCE in 50 mM PBS solution (pH 7.0); scan rate: 100 mV s^{-1}.

biosensor based on the TNT-PANI-GNP has shown superiority over those based on the TNT-PANI and GNP-TNT composites in analytical performance, indicating that PANI as a linker can enhance the contact between GNPs and TNTs, which has in turn improved the analytical characteristics of the biosensor. More specifically, positively charged PANI has strongly adsorbed $AuCl_4^-$ on its surface and significantly improved the deposition of GNPs. In addition, chemical bonding formed between the transition metal titanium and the nitrogen atom in PANI has improved the chemical and electrochemical stability of the ternary composite, which in turn gave rise to the significant enhancement of the electron transfer of HRP and biosensor performance when TNTs-PANI-GNPs replaced TNTs-PANI and GNP-TNTs as the biosensor scaffold.

3.3. Stability, precision, interference and real-life sample analysis

The stability of the TNT-PANI-GNP|[Demim]Br|Nafion|HRP|GCE was investigated by cyclic voltammetry in 50 mM PBS (pH7.0) and the results obtained are shown in Fig. 5. After the electrode potential was repeatedly scanned between 0.15 and −0.45 V at a scan rate of 50 mV s^{-1} for 20 cycles, nearly 96% of the initial peak current was retained and there was also no observable shift in the peak potential, demonstrating the good stability of the modified electrode. In terms of long-term stability, ~94% and ~90% of the initial peak current response was respectively retained after one and three weeks of storage of the modified electrode at 4 °C.

Table 1
Analytical performance of some recent electrochemical HRP biosensors.

HRP biosensors	Linear Range/μM	Detection limit/μM	Sensitivity/μA mM^{-1}	References
ZnO–GNPs–Nafion–HRP/GC	15–1100	9.0	6.0	[42]
HRP/TiO_2 microspheres/Nafion/GC	0.4–140	0.05	20.5	[9]
HRP/GE[a]–CNT–Nafion/AuPt NPs[b]/GCE	0.5–100	0.17	370	[43]
Clay-HRP-Clay/AuCS[c]-GCE	39–3100	9.0	0.57	[44]
Nafion/HRP–GNSs[d]–TiO_2/GCE	41–630	5.9	0.33	[45]
HRP/laponite/Chit[e]/GCE	29–1400	5.0	1.38	[46]
LAM[f]-CS[g]@HRP/dpAu[h]/GCE	2.5–2900	0.83	0.595	[47]
GNP-TNT|HIL|HRP|GCE	15–750	2.2	2.35	[14]
thiolated HRP-GNP-PTA-TNT| RTIL|Nafion|GCE	65–1600	5	18.1	[10]
TNT-PANI-GNP|[Demim]Br |Nafion|HRP|GCE,	1–1225	0.13	22.7	This work

[a] Graphene.
[b] Gold-platinum alloy nanoparticles.
[c] Gold nanoparticles stabilised by chitosan.
[d] Gold nano-seeds.
[e] Chitosan.
[f] L-arginine.
[g] Chitosan.
[h] Gold nanocrystal film.

The repeatability of the biosensor was evaluated by 8 successive measurements in the presence of 0.2 mM H_2O_2 and a relative standard deviation of 1.6% was obtained. Meanwhile, the reproducibility was studied based on the detection signals at six biosensors (fabricated in the same batch) in 0.2 mM H_2O_2 and a relative standard deviation of 5.3% was obtained. Both tests have demonstrated a good precision of the biosensors.

In the present work, the improved stability, prolonged life span and satisfactory precision of the TNT-PANI-GNP|[Demim]Br|Nafion|HRP|GCE are attributed to the advantages of thiolated HRP and TNTs-PANI-GNPs. The strong interaction between sulfhydryl of thiolated HRP and GNPs has minimised the leakage of the enzyme molecules from the biosensor, which has benefited the stability and precision of the biosensors. Furthermore, TNT-PANI has aided in dispersive, rather than agglomerated deposition of GNPs, which would retain the bioactivity of HRP molecules and therefore prolong the life span of the biosensors.

The interference to determination of H_2O_2 by the biosensors was studied using several commonly coexisting interferences including ascorbic acid, dopamine, uric acid and cysteine. In this experiment, the concentration of the interfering species was deliberately set at that of H_2O_2 of 0.2 mM, although their existing level in real-life samples is generally not expected to be higher than that of analytes, so that their maximum interference can be studied. The results showed that the amperometric responses fluctuated by 4.1%, 3.2%, 1.4% and 0.35% after spiking 0.2 mM of each of the interferences listed above into 0.2 mM H_2O_2 solution respectively, indicating a high selectivity and strong anti-interference ability of the TNT-PANI-GNP |[Demim]Br|Nafion|HRP|GCE.

Next, the analytical performance of the biosensor was evaluated by quantitatively determining H_2O_2 in several local disinfectant and urine samples and the results are displayed in Table 2. The disinfectant samples were diluted 1000 times and the human urine samples were diluted ten times with PBS (this was defined in line 178) (pH 7.4) to reduce matrix complexity. Some auto-oxidisable molecules in urine were reportedly able to produce H_2O_2 through rapid superoxide dependent auto-oxidation reactions on exposure to air [41]. In this table, H_2O_2 before spiking was detected by $KMnO_4$ titration method. After the samples were spiked by known standard H_2O_2 solutions, the TNT-PANI-GNP|[Demim]Br|Nafion|HRP|GCE was applied to detect the total concentration of H_2O_2 in the spiked solutions. A 97.6%–104.0% recovery range was obtained for spiked disinfectant samples and 96.8%–105.6% for urine samples, demonstrating the feasibility of the biosensor for the detection of H_2O_2 in real-life samples.

4. Conclusions

In this work, a ternary TNT-PANI-GNP composite has been synthesised and characterised by XRD, FT-IR, TEM, SAED and EIS. The microscopic results have demonstrated that TNTs were encapsulated by the PANI and GNPs were evenly deposited on TNTs-PANI. In this composite, PANI can not only improve the deposition of GNPs by electrostatic adsorption of $AuCl_4^-$, but also enhance the conductivity of the TNTs. Then, voltammetric performance of the TNT-PANI-GNP composite modified electrodes showed that the composite has facilitated the direct electron transfer of HRP to catalyse the reduction of H_2O_2. In our work, HRP was thiolated to enhance their interaction with GNPs and thus minimise their leakage from the biosensors, which has significantly improved the stability, precision and life span of the biosensors. Most importantly, the analytical performance of HRP at the TNT-PANI-GNP|[Demim]Br|Nafion|HRP|GCE has shown superiority over that of other reported HRP biosensors, which was attributed to the excellent biocompatibility and porous geometry of TNTs, strong electrostatic binding ability and good conductivity of PANI, and excellent biocompatibility and conductivity of GNPs.

Table 2
Detection of H_2O_2 in disinfectant samples (1–3) and in urine samples (4–6).

Sample	Detected[a]/mM	Added/mM	Found[b]/mM	Recovery/%	RSD/%
1	0.101	0.100	0.209	104	2.1
2	0.103	0.150	0.247	97.6	2.9
3	0.0980	0.200	0.302	101	2.7
4	0.0180	0.000	0.0190	105	4.4
5	0.119	0.100	0.122	102	4.1
6	0.221	0.200	0.214	96.8	3.6

[a] Detected using $KMnO_2$ oxidation method [48].
[b] Detected at TNT-PANI-GNP|[Demim]Br |Nafion|HRP|GCE.

Conflict of interest

The authors declare no competing financial interest.

Acknowledgements

This work was financially supported by National Natural Science Foundation of China (No. U1504215) and the Scientific Research Foundation for the Returned Overseas Chinese Scholars, State Education Ministry (Batch 46th).

References

[1] B. O'Regan, M. Gratzel, A low-cost, high-efficiency solar cell based on dye-sensitized colloidal TiO_2 films, Nature 353 (6346) (1991) 737–740.
[2] L. Schmidt-Mende, et al., Organic dye for highly efficient solid-state dye-sensitized solar cells, Adv. Mater. 17 (7) (2005) 813–815.
[3] W.J. Bae, et al., One-pot synthesis of hybrid TiO_2-polyaniline nanoparticles by self-catalyzed hydroamination and oxidative polymerization from TiO_2-methacrylic acid nanoparticles, Chem. Commun. 47 (38) (2011) 10710–10712.
[4] C. Lai, et al., Enhanced high-rate capability of the CN-doped TiO_2 as anode material for lithium-ion battery, Electrochem. Solid-State Lett. 15 (5) (2012) A65–A67.
[5] S.G. Pawar, et al., Room temperature ammonia gas sensor based on polyaniline-TiO nanocomposite, Sens. J. IEEE 11 (12) (2011) 3417–3423.
[6] S. Bhadra, et al., Progress in preparation, processing and applications of polyaniline, Prog. Polym. Sci. 34 (8) (2009) 783–810.
[7] A. Katoch, et al., Synthesis of polyaniline/TiO_2 hybrid nanoplates via a sol-gel chemical method, Chem. Eng. J. 192 (0) (2012) 262–268.
[8] X. Li, et al., Preparation of polyaniline-modified TiO_2 nanoparticles and their photocatalytic activity under visible light illumination, Appl. Catal. B Environ. 81 (3) (2008) 267–273.
[9] Q. Xie, et al., Nanosheet-based titania microspheres with hollow core-shell structure encapsulating horseradish peroxidase for a mediator-free biosensor, Biomaterials 32 (27) (2011) 6588–6594.
[10] X. Liu, et al., Gold nanoparticle encapsulated-tubular TiO_2 nanocluster as a scaffold for development of thiolated enzyme biosensors, Anal. Chem. 85 (9) (2013) 4350–4356.
[11] H. Cetin, et al., Electrical characterization of heterojunction between polyaniline titanium dioxide tetradecyltrimethylammonium bromide and n-silicon, Synth. Met. 161 (21–22) (2011) 2384–2389.
[12] W. Tang, L. Li, X. Zeng, A glucose biosensor based on the synergistic action of nanometer-sized TiO_2 and polyaniline, Talanta 131 (0) (2015) 417–423.
[13] B.-S. Kim, et al., In situ template polymerization of aniline on the surface of negatively charged TiO_2 nanoparticles, Synth. Met. 159 (13) (2009) 1369–1372.
[14] X. Liu, et al., Hydrogen peroxide detection at a horseradish peroxidase biosensor with a Au nanoparticle-dotted titanate nanotube|hydrophobic ionic liquid scaffold, Biosens. Bioelectron. 32 (1) (2012) 188–194.
[15] S. Liu, et al., A feasible approach to the fabrication of gold/polyaniline nanofiber composites and its application as electrocatalyst for oxygen reduction, Mater. Chem. Phys. 132 (2–3) (2012) 500–504.
[16] J.M. Fowler, M.C. Stuart, D.K.Y. Wong, Self-assembled layer of thiolated protein G as an immunosensor scaffold, Anal. Chem. 79 (1) (2007) 350–354.
[17] W. Yan, et al., A super highly sensitive glucose biosensor based on Au nanoparticles–AgCl@polyaniline hybrid material, Biosens. Bioelectron. 23 (7) (2008) 925–931.
[18] S.B. Teli, et al., Preparation, characterization and antifouling property of polyethersulfone–PANI/PMA ultrafiltration membranes, Desalination 299 (2012) 113–122.

[19] M.B. Mohamed, K. El-Sayed, Structural, magnetic and dielectric properties of (PANI)-$Ni_{0.5}Zn_{0.5}Fe_{1.5}Cr_{0.5}O_4$ nanocomposite, Compos. Part B Eng. 56 (2014) 270–278.
[20] S. Kant, S. Kalia, A. Kumar, A novel nanocomposite of polyaniline and $Fe_{0.01}Ni_{0.01}Zn_{0.98}O$: photocatalytic, electrical and antibacterial properties, J. Alloys Compd. 578 (2013) 249–256.
[21] A. Elsanousi, et al., Hydrothermal treatment duration effect on the transformation of titanate nanotubes into nanoribbons, J. Phys. Chem. C 111 (39) (2007) 14353–14357.
[22] R. Rajaramakrishna, et al., Nonlinear optical studies of lead lanthanum borate glass doped with Au nanoparticles, J. Non-Crystalline Solids 358 (14) (2012) 1667–1672.
[23] A. Rajan, M. MeenaKumari, D. Philip, Shape tailored green synthesis and catalytic properties of gold nanocrystals, Spectrochim. Acta Part A Mol. Biomol. Spectrosc. 118 (2014) 793–799.
[24] S. Srivastava, et al., Synthesis and characterization of TiO_2 doped polyaniline composites for hydrogen gas sensing, Int. J. Hydrogen Energy 36 (10) (2011) 6343–6355.
[25] A.A. Athawale, M.V. Kulkarni, V.V. Chabukswar, Studies on chemically synthesized soluble acrylic acid doped polyaniline, Mater. Chem. Phys. 73 (1) (2002) 106–110.
[26] Y. Duan, et al., On the correlation between structural characterization and electromagnetic properties of doped polyaniline, Solid State Sci. 12 (8) (2010) 1374–1381.
[27] X. Liu, et al., Evaluation of a carbon nanotube-titanate nanotube nanocomposite as an electrochemical biosensor scaffold, Biosens. Bioelectron. 66 (0) (2015) 208–215.
[28] M. Zhang, et al., Effect of annealing temperature on morphology, structure and photocatalytic behavior of nanotubed $H_2Ti_2O_4(OH)_2$, J. Mol. Catal. A Chem. 217 (1) (2004) 203–210.
[29] I. Paramasivam, J.M. Macak, P. Schmuki, Photocatalytic activity of TiO_2 nanotube layers loaded with Ag and Au nanoparticles, Electrochem. Commun. 10 (1) (2008) 71–75.
[30] H. Zhang, et al., P_{25}-graphene composite as a high performance photocatalyst, ACS Nano 4 (1) (2009) 380–386.
[31] M.R. Karim, et al., Preparation of conducting polyaniline/TiO_2 composite submicron-rods by the γ-radiolysis oxidative polymerization method, React. Funct. Polym. 68 (9) (2008) 1371–1376.
[32] M. Oh, S. Kim, Synthesis and electrochemical analysis of polyaniline/TiO_2 composites prepared with various molar ratios between aniline monomer and para-toluenesulfonic acid, Electrochim. Acta 78 (0) (2012) 279–285.
[33] M.R. Karim, et al., Sulfonated polyaniline-titanium dioxide nanocomposites synthesized by one-pot UV-curable polymerization method, Synth. Met. 159 (3–4) (2009) 209–213.
[34] M. Irimia-Vladu, et al., Vacuum-processed polyaniline–C_{60} organic field effect transistors, Adv. Mater. 20 (20) (2008) 3887–3892.
[35] Q. Tan, et al., Preparation and electrochemical properties of the ternary nanocomposite of polyaniline/activated carbon/TiO_2 nanowires for supercapacitors, Electrochim. Acta 88 (0) (2013) 526–529.
[36] A.G. Yavuz, A. Gok, Preparation of TiO_2/PANI composites in the presence of surfactants and investigation of electrical properties, Synth. Met. 157 (4) (2007) 235–242.
[37] P. Boomi, et al., Study on antibacterial activity of chemically synthesized PANI-Ag-Au nanocomposite, Appl. Surf. Sci. 300 (2014) 66–72.
[38] J.-Z. Xu, et al., Fabricating gold nanoparticle-oxide nanotube composite materials by a self-assembly method, J. Colloid Interface Sci. 290 (2) (2005) 450–454.
[39] J. Yang, et al., Study on composition, structure and formation process of nanotube $Na_2Ti_2O_4(OH)_2$, Dalton Trans. (20) (2003) 3898–3901.
[40] Y. Xiao, H.-X. Ju, H.-Y. Chen, Direct electrochemistry of horseradish peroxidase immobilized on a colloid/cysteamine-modified gold electrode, Anal. Biochem. 278 (1) (2000) 22–28.
[41] A.K. Dutta, et al., Single source precursor approach to the synthesis of Bi_2S_3 nanoparticles: A new amperometric hydrogen peroxide biosensor, Sens. Actuators B Chem. 192 (2014) 578–585.
[42] C. Xiang, et al., Direct electrochemistry and enhanced electrocatalysis of horseradish peroxidase based on flowerlike ZnO–gold nanoparticle–Nafion nanocomposite, Sens. Actuators B Chem. 136 (1) (2009) 158–162.
[43] Q. Sheng, M. Wang, J. Zheng, A novel hydrogen peroxide biosensor based on enzymatically induced deposition of polyaniline on the functionalized graphene–carbon nanotube hybrid materials, Sens. Actuators B Chem. 160 (1) (2011) 1070–1077.
[44] X. Zhao, et al., Direct electrochemistry and electrocatalysis of horseradish peroxidase based on clay–chitosan-gold nanoparticle nanocomposite, Biosens. Bioelectron. 23 (7) (2008) 1032–1038.
[45] Y. Wang, et al., Direct electrochemistry and bioelectrocatalysis of horseradish peroxidase based on gold nano-seeds dotted TiO2 nanocomposite, Biosens. Bioelectron. 25 (11) (2010) 2442–2446.
[46] D. Shan, et al., Reagentless biosensor for hydrogen peroxide based on self-assembled films of horseradish peroxidase/laponite/chitosan and the primary investigation on the inhibitory effect by sulfide, Biosens. Bioelectron. 26 (2) (2010) 536–541.
[47] Q. Chen, et al., The application of chiral arginine and multi-walled carbon nanotubes as matrices to monitor hydrogen peroxide, Bioelectrochemistry 91 (0) (2013) 32–36.
[48] N.V. Klassen, D. Marchington, H.C.E. McGowan, H_2O_2 Determination by the I_3^- method and by $KMnO_4$ titration, Anal. Chem. 66 (18) (1994) 2921–2925.